Model Predictive Control of a Three-Phase Two-Level Four-Leg Grid-Connected Converter Based on Sphere Decoding Method

Bo Long, *Senior Member, IEEE*, Tianxu Cao, Wenting Fang, Kil To Chong, *Member, IEEE*, and Josep M. Guerrero, *Fellow, IEEE*

***Abstract*—To achieve optimal control of four-leg grid-connected converters in terms of switching frequency and current tracking, the finite-control-set model-predictive-control method (FCS-MPC) can be applied. In this method, the cost function (CF) considers tracking control of grid current, filter capacitance voltage, and converter-side current as well as switching frequency before allocating different weights in its calculations. Thus, multiobjective optimization is achieved by trying to find the optimal switching sequence that minimizes the CF. However, as the horizon length is increased, the solution search enlarges exponentially, soon requiring an exhaustive search through each of many candidates. To alleviate this computational burden, this article presents an FCS-MPC method that is based on a new node-comparison sphere decoding method (NC-SDM), thereby reformulating the CF minimization problem into an integral-least-squares problem. The proposed NC-SDM reduces the computational burden associated with longer horizons by excluding as many suboptimal solutions from the candidates as possible. It does this by continuously comparing the length of two paths corresponding to each node of the search tree, and always taking the branch with shorter length. The final length of the total path is set as the initial radius after superposing all the path lengths. As a result, the initial radius estimation is much smaller than that in the Babai method and the computational cost is further reduced. Finally, simulation and experimental results validate the feasibility and suitability of the proposed method.**

***Index Terms*—Cost function (CF), finite-control-set (FCS) model predictive control, node comparison method, three-phase four-leg grid-connected converter (GCC).**

Manuscript received December 31, 2019; revised April 16, 2020; accepted June 28, 2020. Date of publication July 2, 2020; date of current version September 22, 2020. This work was supported in part by the Fundamental Research Funds for the Central Universities of China (ZYGX2019J033), in part by the National Natural Science Foundation of China under Grant 51975453, in part by Key R&D Plan of Science and Technology Department of Sichuan Province (20ZDYF2816), in part by the State Key Laboratory of Control and Simulation of Power System Generation Equipment, Tsinghua University, China (SKLD20M11), and in part by The VELUX FOUNDATIONS under the VILLUM Investigator Grant Center for Research on Microgrids under Award No. 25920. Recommended for publication by Associate Editor J. Rodriguez. *(Corresponding author: Bo Long.)*

Bo Long, Tianxu Cao, and Wenting Fang are with the School of Mechanical and Electrical Engineering, Institute of Electric Vehicle Driving System and Safety Technology, University of Electronic Science and Technology of China, Chengdu 611731, China (e-mail: longbouestc1980@126.com; 1011901845@qq.com; 2494176858@qq.com).

Kil To Chong is with the Department of Electronics and Information Engineering, Jeonbuk National University, Jeonju 54896, South Korea (e-mail: kitchong@jbnu.ac.kr).

Josep M. Guerrero is with the Department of Energy Technology, Aalborg University, DK-9220 Aalborg, Denmark (e-mail: joz@et.aau.dk).

Color versions of one or more of the figures in this article are available online at https://ieeexplore.ieee.org.

Digital Object Identifier 10.1109/TPEL.2020.3006432

I. Introduction

THREE-PHASE four-leg grid-connected converters (GCCs) act as a bridge to convert dc power into high-quality ac power, which is an important element of distributed power generation systems based on renewable energy (RE) (e.g., wind energy and solar energy). As a result, high-performance control and power quality management for GCCs is an important research topic in RE [1], [2]. Many international standards have given detailed requirements on the power quality required of RE sources that are connected to electric utilities [3]–[5].

The typical power circuit for traditional GCCs is composed of a three-phase two-level power converter with six switching devices. There are abundant switching harmonics in grid current because of the pulsewidth modulation (PWM) modulation technique used. To filter out the majority of these harmonics, *LCL* filters are used, and they were designed to provide sufficient attenuation for harmonic current in order to comply with grid standards. However, these filters bring additional resonance issues that must be properly damped to guarantee the system stability [6]–[8].

The problem for conventional three-leg GCCs is that they do not achieve good performance for loads that contain a neutral line or for unbalanced loads. Moreover, GCCs can generate dc-link current ripples that degrade the service life of dc-link capacitors in GCCs [9]. Motivated by this, a two-level four-leg GCCs that can provide greater control flexibility and an improvement in output voltage/current quality is proposed. The advantages of three-phase four-leg GCCs are as follows:

1) They can simultaneously provide voltage for three-phase and single-phase loads.
2) Their dc-link capacitance can be smaller than that of three-leg GCCs.
3) For four-leg converters, there is no need for voltage balance control strategies.
4) They give much higher dc-link voltage utilization capability.
5) They are more flexible in terms of voltage and current control since they have an additional degree-of-freedom in control; this can give direct control over the zero-sequence voltage for loads they manage [10]–[12].

Many methods have been applied for current control in four-leg GCCs [13], [14]. Proportion-integral-derivative (PID) controllers have been widely applied and are relatively simple to implement [15]; however, PID controllers come with inherent steady-state errors and poor dynamic performance. Generally, a controller is regulated by the feedback of the current outer loop, which is sensitive to certain parameters; this makes their system design and parameter selection very complex [16]. The H_∞ control method, which is robust to uncertain parameters, has also gained interest due to the stability control improvements it gives GCCs [17], [18]. Despite this promise, the design of H_∞ robust controller needs complex mathematic calculations, making it difficult for engineers to work with. Sliding mode control, which has the merits of being robust under disturbances, has also been applied to GCCs [19]–[21]; however, this has serious problems that come from chatting issues. In [22], an artificial neural network (NN) was proposed for GCCs that achieved good performance under disturbances. However, the method relied upon a microcontroller with very fast computational capability to work. In a word, these methods usually need to control the active and reactive power by decoupling the grid current under *dq* coordinates, which means that complicated coordinate transformations are required.

Finite-control-set model-predictive-control method (FCS-MPC) has been a very popular prediction control method for electronic systems in recent years [23], [24]. In contrast to conventional control methods, it is based on a fundamentally different control principle. Instead of designing the loop controller for every controlled variable and then cascading them together, it utilizes a discrete-time model of GCCs with an *LCL* filter to predict the future behavior of all possible control inputs before choosing the appropriate switching sequence to minimize its cost function (CF) that is based on the square of the Euclidean distance between the reference signal and feedback variables [25], [26].

The available literature shows that much of the previous work on MPC control of three-phase four-leg inverters has already been completed [24], [26], [27]. In [28] and [29], the MPC of an *LC* three-phase four-leg grid-connected inverter in islanded-grid environment was studied. Using this as a basis, the FCS-MPC method under quasi-Z source and unbalanced loads was studied [30]. In [31], based on the designed CF, a constrained MPC based on an NN was adopted to realize optimal control of the output duty cycle. In [32], a Lyapunov-based model of predictive control was adopted to comprehensively consider the tracking error, total harmonic distortion (THD), and calculation expense of three-phase four-leg GCCs.

In four-leg GCCs, the FC-MPC is realized without an internal proportional-integral current controller and PWM modulation stage; these items can take several variables (e.g., grid current tracking error, THD, and switching losses) into account. Taking the switching sequence of the next few cycles as the variable, the switching sequence is obtained by calculating the lowest CF, which is constructed through weight factor allocation. The first switch sequence is used as the control sequence of the inverter. If the weight factors are reasonable and the prediction horizon is longer, the MPC control can consider the controlled quantity better and control the steady-state dynamic performance better. As a result, switching frequency in an MPC is much lower than in the conventional control methods. However, longer prediction horizons incur larger computational costs on the microprocessor, and increase the computational expense of the embedded system. To alleviate this computational burden, in this article, a novel sphere decoding algorithm based on a node comparison method is introduced; this approach is realized by transforming the CF into a standard form of a sphere decoding algorithm. Thus, the CF minimization problem is reformulated into an integral-least-squares (ILS) problem. The main contributions of this article are summarized as follows.

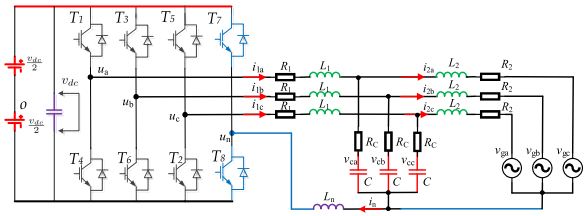

Fig. 1. Topology of the two-level four-leg GCCs with an *LCL* filter.

1) The operation principle and prediction model for a two-level four-leg GCC are established.
2) The steps for reformulating the CF minimization problem into an ILS problem are explained.
3) Considering the calculation expense of sphere decoding is closely related to the initial radius selection, based on the Babai estimation method in [33], a novel method, named the "node comparison method," that can further reduce the initial radius and the tree searching time for the optimal switching sequence is introduced.

The rest of this article is organized as follows. Section II presents the operation principle and discrete-time prediction model for three-phase four-leg GCCs with an *LCL* filter. In Section III, the FC-MPC control for four-leg GCCs is proposed. A CF that considers grid current tracking errors and switching losses is presented. To alleviate the calculation expense involved in a multistep prediction, the tree searching time for the optimal switching sequence is alleviated by a sphere decoding method. Step-by-step demonstrations on reformulating the CF minimization problem into an ILS problem are discussed. Furthermore, both Babai estimation and node comparison methods are presented for initial radius selection. Section IV shows the simulation results. Section V gives the experimental results to validate the proposed control method. Finally, the conclusion is summarized in Section VI.

II. Three-Phase Two-Level Four-Leg GCCs

A. Operation of the Four-Leg GCCs

The topology of a GCC for distributed generation (DG) is depicted in Fig. 1; the system consists of a three-phase four-leg converter, an *LCL* filter, and the grid. Here, $v_{\rm dc}$ is the dc-link voltage, v_{ga}, v_{gb}, and v_{gc} are the grid voltages, L_1 is the grid voltage, i_{1a}, i_{1b}, and i_{1c} are inverter side currents, i_{2a}, i_{2b}, and i_{2c} are the grid side currents, v_{ca}, v_{cb}, and v_{cc} are the

capacitor voltages, and i_n is the neutral line current. L_2 is the grid side inductance, C is the filter capacitance, and R_1 and R_2 represent the parasitic resistances of L_1 and L_2, respectively. This connection is similar to that of a conventional three-phase three-wire converter, but an additional leg has been connected to the neutral point of the grid, which allows control of zero-sequence current/voltage.

It is assumed that the switching components of the system are ideal. At any given instance, each phase of the system may only assume one of two possible switching states contained in the finite control set as

$$\boldsymbol{u}(k) = [u_a, u_b, u_c, u_n]^T \tag{1}$$

where $u_a, u_b, u_c, u_n \in (-1, 1)$. "$u = 1$" means that the upper bridge power transistor is in the ON state, and the lower bridge power transistors are in the OFF state. "$u = -1$" means that the lower bridge switches are ON and the upper bridge switches are OFF.

B. Discrete Model

To get the discrete-time state-space equation of the four-leg GCCs, we compose the continuous-time state variable $\boldsymbol{x}(t)$ that contains the converter-side current $\boldsymbol{i}_1(t)$, grid-side current $\boldsymbol{i}_2(t)$, and the filter-capacitor voltage $\boldsymbol{v_c}(t)$; this is defined as $\boldsymbol{x}(t) = [\boldsymbol{i}_1(t), \boldsymbol{v_c}(t), \boldsymbol{i}_2(t)]^T$, where $\boldsymbol{i}_1(t)$, $\boldsymbol{i}_2(t)$, $\boldsymbol{v_c}(t)$, and the grid voltage $\boldsymbol{e_g}(t)$ are given by

$$\begin{cases} \boldsymbol{i}_1\ (t) = [i_{1a}, i_{1b}, i_{1c}]^T \\ \boldsymbol{i}_2\ (t) = [i_{2a}, i_{2b}, i_{2c}]^T \\ \boldsymbol{v_c}\ (t) = [v_{ca}, v_{cb}, v_{cc}]^T \\ \boldsymbol{e_g}\ (t) = [e_{ga}, e_{gb}, e_{gc}]^T \\ v\ = [v_{an}, v_{bn}, v_{cn}]^T. \end{cases} \tag{2}$$

Assuming $\boldsymbol{u}$ represents the switching state of each leg, according to Kirchhoff's law, the circuit equation for converter-side inductance L_1, grid-side inductance L_2, and filter capacitance $C_{\boldsymbol{f}}$ can be derived as:

$$\begin{cases} \boldsymbol{L_{eq}} \frac{d\boldsymbol{i}_1}{dt} + R_C C \frac{d\boldsymbol{v_c}}{dt} = -\boldsymbol{v_c} + \frac{V_D}{2} M u \\ L_2 \frac{d\boldsymbol{i}_2}{dt} - R_C C \frac{d\boldsymbol{v_c}}{dt} = \boldsymbol{v_c} - \boldsymbol{v_g} \\ \frac{d\boldsymbol{v_c}}{dt} = \frac{1}{C}\boldsymbol{i}_1 - \frac{1}{C}\boldsymbol{i}_2 \end{cases} \tag{3}$$

where

$$\boldsymbol{L_{eq}} = \begin{bmatrix} L_1 + L_n & L_n & L_n \\ L_n & L_1 + L_n & L_n \\ L_n & L_n & L_1 + L_n \end{bmatrix}$$

$$\boldsymbol{M} = \begin{bmatrix} 1 & 0 & 0 & -1 \\ 0 & 1 & 0 & -1 \\ 0 & 0 & 1 & -1 \end{bmatrix}.$$

Thus, the continuous-time state-space model in (3) can be simplified as

$$\begin{cases} \alpha \frac{d\boldsymbol{x}(t)}{dt} = \beta x(t) + \gamma u(t) + \delta \boldsymbol{e}_g(t) \\ y\ (k) = Cx(t) \end{cases} \tag{4}$$

where $\boldsymbol{C} = [\lambda_1\ \lambda_2\ \lambda_3]$ is the weight factor for the inverter-side current $\boldsymbol{i}_1$, the grid-side current $\boldsymbol{i}_2$, and the capacitor voltage $\boldsymbol{v_c}$. Then, $\boldsymbol{y} = [\lambda_1 \boldsymbol{i}_1\ \lambda_2 \boldsymbol{i}_2\ \lambda_3 \boldsymbol{v}_c]^{\boldsymbol{T}}$, $\boldsymbol{y}(t)$ is the weight redistribution of the state variable $\boldsymbol{x}(t)$.$\boldsymbol{u} = [T_a\ T_b\ T_c\ T_n]^{\boldsymbol{T}}$, $\boldsymbol{\alpha}$, $\boldsymbol{\beta}$, $\boldsymbol{\gamma}$, and $\boldsymbol{\delta}$ are all constant matrices. T_a, T_b, T_c, and T_n are the duty ratios of the upper four legs. By assuming that $\boldsymbol{I}_{i\times i}$ is the ith order unit matrix, $\boldsymbol{O}_{i\times j}$ is an empty matrix with i rows and j columns, and $\boldsymbol{\alpha}$, $\boldsymbol{\beta}$, $\boldsymbol{\gamma}$, and $\boldsymbol{\delta}$ can be expressed by

$$\boldsymbol{\alpha} = \begin{pmatrix} \boldsymbol{L_{eq}} & RC.\boldsymbol{I}_{3\times3} & \boldsymbol{O}_{3\times3} \\ \boldsymbol{O}_{3\times3} & C.\boldsymbol{I}_{3\times3} & \boldsymbol{O}_{3\times3} \\ \boldsymbol{O}_{3\times3} & RC.\boldsymbol{I}_{3\times3} & -L_2.\boldsymbol{I}_{3\times3} \end{pmatrix}$$

$$\boldsymbol{\beta} = \begin{pmatrix} \boldsymbol{O}_{3\times3} & -\boldsymbol{I}_{3\times3} & \boldsymbol{O}_{3\times3} \\ \boldsymbol{I}_{3\times3} & \boldsymbol{O}_{3\times3} & -\boldsymbol{I}_{3\times3} \\ \boldsymbol{O}_{3\times3} & -\boldsymbol{I}_{3\times3} & \boldsymbol{O}_{3\times3} \end{pmatrix}$$

$$\boldsymbol{\gamma} = \begin{pmatrix} \boldsymbol{V_{dc}} & 0 & 0 & \\ 0 & \boldsymbol{V_{dc}} & 0 & \boldsymbol{O}_{4\times6} \\ -\boldsymbol{V_{dc}} & -\boldsymbol{V_{dc}} & -\boldsymbol{V_{dc}} & \end{pmatrix}^{\boldsymbol{T}}$$

$$\boldsymbol{\delta} = \boldsymbol{C}^{\boldsymbol{T}} = (\boldsymbol{O}_{3\times6}\, \boldsymbol{I}_{3\times3})^{\boldsymbol{T}}.$$

Equation (4) can be changed into the standard form of a state-space equation given as

$$\begin{cases} \frac{d\boldsymbol{x}(t)}{dt} = Fx(t) + Gu(t) + P\boldsymbol{e}_g(t) \\ y\ (t) = Cx(t) \end{cases} \tag{5}$$

where $\boldsymbol{F}$, $\boldsymbol{G}$, and $\boldsymbol{P}$ are the parameter matrices of the circuit, $\boldsymbol{F} = \boldsymbol{\alpha}^{-1} \times \boldsymbol{\beta}, \boldsymbol{G} = \boldsymbol{\alpha}^{-1}\boldsymbol{\gamma}$, and $\boldsymbol{P} = \boldsymbol{\alpha}^{-1}\boldsymbol{\delta}$. By using the Du Hamel formula [34] to discretize (5), the discretized-time state-space equation can be obtained as

$$\begin{cases} x\ (k+1) = Ax(k) + Bu(k) + T\boldsymbol{v}_g(k) \\ y\ (k) = Cx(k) \end{cases} \tag{6}$$

where

$$\boldsymbol{A} = e^{\boldsymbol{F}T_s}, \boldsymbol{B} = -\boldsymbol{F}^{-1}(\boldsymbol{I} - \boldsymbol{A})\boldsymbol{G}, \text{ and } \boldsymbol{T} = -\boldsymbol{F}^{-1}(\boldsymbol{I} - \boldsymbol{A})\boldsymbol{P}.$$

Since $\boldsymbol{x}(k)$ and $\boldsymbol{v}_g(k)$ at the kth instant can be measured, the instant state variable $\boldsymbol{x}(k+m)$ can be derived as

$$\begin{cases} x\ (k+1) = Ax(k) + Bu(k) + T\boldsymbol{v}_g(k) \\ x\ (k+2) = \boldsymbol{A}^2 x(k) + ABu(k) + Bu(k+1) \\ +AT\boldsymbol{v}_g(k) + T\boldsymbol{v}_g(k+1) \\ x\ (k+m) = \boldsymbol{A}^m x(k) + \boldsymbol{A}^{m-1}Bu(k) \\ +\cdots + \boldsymbol{A}^0 Bu(k+m-1) + \boldsymbol{A}^0 T\boldsymbol{v}_g(k+m-1). \end{cases} \tag{7}$$

The output equation of the system can be written as

$$\boldsymbol{y}(k+m) = \boldsymbol{C}\boldsymbol{x}\ (k+m) = \boldsymbol{C}\boldsymbol{A}^m \boldsymbol{x}(k) \sum_{l=0}^{m-1} \boldsymbol{C}\boldsymbol{A}^{m-1-l} \times \boldsymbol{B}\boldsymbol{u}(k+\ l) + \sum_{l=0}^{m-1} \boldsymbol{C}\boldsymbol{A}^{m-1-l}\boldsymbol{T}\boldsymbol{v}_g(k+l). \tag{8}$$

According to the discrete-time state-space equations in (7) and (8), the future reference values for $\boldsymbol{i}_1$, $\boldsymbol{i}_2$, and $\boldsymbol{v}_c$ can be prepared for *N* time steps of the horizon; the grid voltage $\boldsymbol{v}_g(k)$ is also filled with its *N* future steps by Lagrange extrapolation method. It is needed to note that digital implementation delay may influence

the prediction model, we suggest that time-delay compensations should be considered in (7) to maintain the prediction model to be closer to the real system. To ensure that the future reference values are correct, we suggest filtering out the grid voltage harmonics before being used in the prediction model. Thus, the references for $\boldsymbol{v}_g(k)$, $\boldsymbol{u}(k)$, and $\boldsymbol{Y}(k)$ can be derived as in (9), and (10) and (11), shown at the bottom of this page

$$\begin{cases} \boldsymbol{V}_g\ (k) = [\boldsymbol{v_g}\,(k)\ \boldsymbol{v_g}\,(k+1)\ \ \cdots\ \ \boldsymbol{v_g}\,(k+N-1)]^T \\ U\ (k) = [\boldsymbol{u}\,(k)\ \ \boldsymbol{u}\,(k+1)\ \ \cdots\ \ \boldsymbol{u}\,(k+m-1)]^T \\ Y\ (k) = [\boldsymbol{y}\,(k+1)\ \ \boldsymbol{y}\,(k+1)\ \ \cdots\ \ \boldsymbol{y}\,(k+m)]^T. \end{cases} \tag{9}$$

At each instant $k,\ k+1, \cdots k+m-1$, the state-space equation at that moment can be derived according to the recursive relation. By integrating these equations according to the vectors in (9), the system output equation that takes the prediction horizon ***N*** into account can be obtained as

$$\boldsymbol{Y}\,(k) = \boldsymbol{\Gamma x}\,(k) + \boldsymbol{\Upsilon U}\,(k) + \boldsymbol{\Psi V}_g\,(k) \tag{12}$$

where

$$\boldsymbol{\Gamma} = \begin{bmatrix} \boldsymbol{CA} & \boldsymbol{CA}^2 & \boldsymbol{CA}^3 & \cdots & \boldsymbol{CA^N} \end{bmatrix}^{\boldsymbol{T}}$$

$$\boldsymbol{Y} = \begin{bmatrix} \boldsymbol{CB} & 0 & \cdots & 0 \\ \boldsymbol{CAB} & \boldsymbol{CB} & \cdots & 0 \\ \vdots & \vdots & \vdots & \vdots \\ \boldsymbol{CA^{N-1}} & \boldsymbol{CA^{N-2}B} & \cdots & \boldsymbol{CB} \end{bmatrix}$$

$$\boldsymbol{\Psi} = \begin{bmatrix} \boldsymbol{CT} & 0 & \cdots & 0 \\ \boldsymbol{CAT} & \boldsymbol{CT} & \cdots & 0 \\ \vdots & \vdots & \vdots & \vdots \\ \boldsymbol{CA^{N-1}T} & \boldsymbol{CA^{N-2}T} & \cdots & \boldsymbol{CT} \end{bmatrix}.$$

In (12), $\boldsymbol{\Gamma}, \boldsymbol{\Upsilon},$ and $\boldsymbol{\Psi}$ are the state matrices related to the ***A, B***, ***C***, and ***T*** matrices, respectively, and they are all time invariant matrices. Conclusions drawn from (9) means that the output vector $\boldsymbol{Y}(k)$ combines the outputs at instant *N* in the future, and they can be obtained recursively from the input $\boldsymbol{x}(k)$ at the moment k. $\boldsymbol{U}(k)$ is the combination of all possible switching sequences adopted at instant *N*. The task of the predictive control of the model is to find the optimal solution of this sequence and apply its first switching sequence sets to the inverter. $\boldsymbol{V}_g(k)$ is the three-phase grid voltage at moment k. Since the *k*th instant was measured and taken out, it is determined in future steps without considering grid voltage fluctuations.

III. Finite-Control-Set Model Predictive Control (FCS-MPC)

A. CF Design

The goal of four-leg *LCL* GCCs is to ensure that the power converter provides high power quality grid current integration to the grid. Meanwhile, power consumption generated due to the switching frequency of the power transistors should be kept to a minimum. In a steady-state, the grid-side current should have only a small tracking error and minor harmonic distortion. The dynamic response of the grid current to phenomena such as overshoot, fast time response, and switching losses, should also been guaranteed. After considering the above factors, the CF is designed as follows:

$$\begin{aligned} J\ =\ & \sum_{l=k}^{k+N-1} (\boldsymbol{y}^*\,(l+1) - \boldsymbol{y}(l+1)^2 \\ & + \lambda_u \boldsymbol{u}\,(l) - \boldsymbol{u}(l-1)^2). \end{aligned} \tag{13}$$

In (13), $\|\cdot\|$stands for the Euclidean 2-norms of the vector, and $\boldsymbol{y}^*$ is the reference value of the output. Due to the steady

$$\begin{aligned} J_A =\ & \|\boldsymbol{\Gamma x}\,(k) + \boldsymbol{\Upsilon U}\,(k) + \boldsymbol{\Psi V}_g\,(k) - \boldsymbol{Y}^*\,(k)\|_2^2 \\ =\ & [\boldsymbol{\Gamma x}\,(k) + \boldsymbol{\Upsilon U}\,(k) + \boldsymbol{\Psi V}_g\,(k) - \boldsymbol{Y}^*\,(k)]^T \cdot [\boldsymbol{\Gamma x}\,(k) + \boldsymbol{\Upsilon U}\,(k) + \boldsymbol{\Psi V}_g\,(k) - \boldsymbol{Y}^*\,(k)] \\ =\ & [\boldsymbol{\Gamma x}\,(k) + \boldsymbol{\Upsilon U}\,(k) - \boldsymbol{Y}^*\,(k)]^T [\boldsymbol{\Gamma x}\,(k) + \boldsymbol{\Upsilon U}\,(k) - \boldsymbol{Y}^*\,(k)] + [\boldsymbol{\Gamma x}\,(k) + \boldsymbol{\Upsilon U}\,(k) - \boldsymbol{Y}^*\,(k)]^T \boldsymbol{\Psi V}_g\,(k) \\ & + [\boldsymbol{\Psi V}_g\,(k)]^{\boldsymbol{T}} [\boldsymbol{\Psi V}_g\,(k)] + [\boldsymbol{\Psi V}_g\,(k)]^T \cdot [\boldsymbol{\Gamma x}\,(k) + \boldsymbol{\Upsilon U}\,(k) - \boldsymbol{Y}^*\,(k)] \\ =\ & \{[\boldsymbol{\Gamma x}\,(k) - \boldsymbol{Y}^*\,(k)]^T [\boldsymbol{\Gamma x}\,(k) - \boldsymbol{Y}^*\,(k)] + [\boldsymbol{\Gamma x}\,(k) - \boldsymbol{Y}^*\,(k)]^T \boldsymbol{\Upsilon U}\,(k) + [\boldsymbol{\Upsilon U}\,(k)]^T [\boldsymbol{\Gamma x}\,(k) - \boldsymbol{Y}^*\,(k)] \\ & + [\boldsymbol{\Upsilon U}\,(k)]^T [\boldsymbol{\Upsilon U}\,(k)]\,\} + 2[\boldsymbol{\Gamma x}\,(k) + \boldsymbol{\Upsilon U}\,(k) - \boldsymbol{Y}^*\,(k)]^T \boldsymbol{\Psi V}_g\,(k) + \boldsymbol{V}_g(k)^T \boldsymbol{\Psi \Psi^T V}_g\,(k) \\ =\ & \|\boldsymbol{\Gamma x}\,(k) - \boldsymbol{Y}^*\,(k)\|_2^2 + 2[\boldsymbol{\Gamma x}\,(k) - \boldsymbol{Y}^*\,(k)]^T [\boldsymbol{\Upsilon U}\,(k)] + \boldsymbol{U}(k)^{\boldsymbol{T}} \left[\boldsymbol{\Upsilon}^{\boldsymbol{T}} \boldsymbol{\Upsilon}\right] \boldsymbol{U}\,(k) \\ & + 2[\boldsymbol{\Gamma x}\,(k) + \boldsymbol{\Upsilon U}\,(k) - \boldsymbol{Y}^*\,(k)]^T \boldsymbol{\Psi V}_g\,(k) + \|\boldsymbol{\Psi V}_g\,(k)\|_2^2 \end{aligned} \tag{10}$$

$$\begin{aligned} J_B =\ & \lambda_u \|\boldsymbol{SU}\,(k) - \boldsymbol{EU}\,(k-1)\|_2^2 = \lambda_u [\boldsymbol{SU}\,(k) - \boldsymbol{EU}\,(k-1)]^T [\boldsymbol{SU}\,(k) - \boldsymbol{EU}\,(k-1)] \\ =\ & \lambda_u \left\{ [\boldsymbol{SU}\,(k)]^T \boldsymbol{SU}\,(k) - [\boldsymbol{SU}\,(k)]^T \boldsymbol{EU}\,(k-1) \right\} - [\boldsymbol{EU}\,(k-1)]^T \boldsymbol{SU}\,(k) + [\boldsymbol{EU}\,(k-1)]^T \boldsymbol{EU}\,(k-1) \\ =\ & \lambda_u \left\{ -[\boldsymbol{SU}\,(k)]^{\boldsymbol{T}} \boldsymbol{EU}\,(k-1) - [\boldsymbol{EU}\,(k-1)]^{\boldsymbol{T}} \boldsymbol{U}\,(k) \right\} + \boldsymbol{U}(k)^{\boldsymbol{T}} \left\{ \lambda_u \boldsymbol{SS^T} \right\} \boldsymbol{U}\,(k) \\ =\ & \lambda_u \|\boldsymbol{EU}\,(k-1)\|_2^2 - 2\lambda_u \left\{ [\boldsymbol{EU}\,(k-1)]^{\boldsymbol{T}} \boldsymbol{SU}\,(k) \right\} + \boldsymbol{U}(k)^{\boldsymbol{T}} \left\{ \lambda_u \boldsymbol{S^T S} \right\} \boldsymbol{U}\,(k) \end{aligned} \tag{11}$$

parameters of the circuit,$\boldsymbol{y}^*$ from k to $k+N-1$ moment is also determined. λ_u is the weight factor for the switching loss. The first term of the CF represents the error between the output reference value and the actual value. The second term deals with the change in switching state, by taking the switching loss into account, and if we substitute (12) into (13), the CF can be written as

$$J = \underbrace{\Gamma x(k) + YU(k) + \Psi V_g(k) - Y^*(k)_2^2}_{J_A} + \underbrace{\lambda_u SU(k) - EU(k-1)_2^2}_{J_B} = J_A + J_B \tag{14}$$

where J_A and J_B can be derived by (10) and (11).

In (15), as shown at bottom of the page, $\boldsymbol{S}$ and $\boldsymbol{E}$ can be written as

$$\mathbf{S} = \begin{bmatrix} \boldsymbol{I}_4 & 0_{4\times4} & \cdots & 0_{4\times4} \\ -\boldsymbol{I}_4 & \boldsymbol{I}_4 & \cdots & 0_{4\times4} \\ 0_{4\times4} & -\boldsymbol{I}_4 & \cdots & 0_{4\times4} \\ \vdots & \vdots & \vdots & \vdots \\ 0_{4\times4} & 0_{4\times4} & \cdots & \boldsymbol{I}_4 \end{bmatrix} \quad \text{and} \quad \boldsymbol{E} = \begin{bmatrix} \boldsymbol{I}_4 \\ 0_{4\times4} \\ 0_{4\times4} \\ \vdots \\ 0_{4\times4} \end{bmatrix}.$$

$\boldsymbol{S}$ and $\boldsymbol{E}$ consist of a zero and an identity matrix dimensioned to be 4×4 in accordance with the three-phase four-leg system. More details can be obtained in [33]. The eight terms in (15) are all added together to produce the CF $\boldsymbol{J}$, which is a constant. Each of these terms are therefore also constants and can be seen as a 1×1 matrix. A 1×1 matrix is a special case for which the following is permitted: $\boldsymbol{J^T L} = (\boldsymbol{J^T L})^{\boldsymbol{T}}$. Therefore, the sixth term in (15) can be manipulated as

$$\begin{aligned} 2[\boldsymbol{\Upsilon U}(k)]^{\boldsymbol{T}} \boldsymbol{\Psi V}_g(k) &= 2\Big\{[\boldsymbol{\Upsilon U}(k)]^{\boldsymbol{T}}[\boldsymbol{\Psi V}_g(k)]\Big\}^T \\ &= 2[\boldsymbol{\Psi V}_g(k)]^T[\boldsymbol{\Upsilon U}(k)] \\ &= 2\boldsymbol{V}_g(k)^{\boldsymbol{T}} \boldsymbol{\Psi}^{\boldsymbol{T}} \boldsymbol{\Upsilon U}(k) \end{aligned} \tag{16}$$

where

$$\boldsymbol{Y}^*(k) = \big[\, \boldsymbol{y}^*(k+1)\ \boldsymbol{y}^*(k+2) \cdots \boldsymbol{y}^*(k+N) \,\big]^T$$

is the reference vector merged at instant N and corresponds to $\boldsymbol{Y}(k)$. $\boldsymbol{u}(k-1)$ is the switching sequence state during the previous step. $\boldsymbol{S}$ and $\boldsymbol{E}$ are invariant matrices.

According to the CF defined in (13), once optimal control is achieved, the CF reaches its minimum, then the voltage vector $\boldsymbol{U}(k)$ gives the optimum switching sequence

$$\boldsymbol{U}_{\text{opt}}(k) = \arg\min_{\boldsymbol{U}(k)} J. \tag{17}$$

Closed-loop management of the model's predictive control is accomplished by taking the first group of switching states $\boldsymbol{U}_{\text{opt}}(k)$ as the input. To simplify the calculation in (15), the CF needs to be split and merged, and is sorted as in the following:

$$\begin{aligned} J &= \theta(k) + 2\boldsymbol{\Theta}(k)\boldsymbol{U}(k) + \boldsymbol{U}^T(k)\boldsymbol{Q}\boldsymbol{U}(k) \\ &= \theta(k) + 2\boldsymbol{\Theta}(k)\boldsymbol{U}(k) + \|\boldsymbol{U}(k)\|_Q^2 \end{aligned} \tag{18}$$

where

$$\begin{aligned} \theta(k) &= \|\boldsymbol{\Gamma x}(k) - \boldsymbol{Y}^*(k)\|_2^2 + \|\boldsymbol{\Psi V}_g(k)\|_2^2 \\ &\quad + \lambda_u \|\boldsymbol{EU}(k-1)\|_2^2 + 2[\boldsymbol{\Gamma x}(k) - \boldsymbol{Y}^*(k)]^T \boldsymbol{\Psi V}_g(k) \\ \boldsymbol{\Theta}(k) &= \{[\boldsymbol{\Gamma x}(k) - \boldsymbol{Y}^*(k)]^T \boldsymbol{\Upsilon} + \boldsymbol{V}_g(k)^{\boldsymbol{T}} \boldsymbol{\Psi}^{\boldsymbol{T}} \boldsymbol{\Upsilon} \\ &\quad - \lambda_u \Big\{[\boldsymbol{EU}(k-1)]^{\boldsymbol{T}} \boldsymbol{S}\Big\}^T \\ \boldsymbol{Q} &= \boldsymbol{\Upsilon}^{\boldsymbol{T}} \boldsymbol{\Upsilon} + \lambda_u \boldsymbol{S}^{\boldsymbol{T}} \boldsymbol{S} \end{aligned}$$

where $\boldsymbol{Q}$ is symmetric and positive definite, hereby a vector ξ weighted with the matrix $\boldsymbol{Q}$ is given by $\boldsymbol{\xi}_{\boldsymbol{Q}}^2 = \boldsymbol{\xi}^{\boldsymbol{T}} \boldsymbol{Q} \boldsymbol{\xi}$. Only the first two variables of the new CF, namely $\theta(k)$ and $\Theta(k)$, change due to the inclusion of the grid voltage as an input vector $\boldsymbol{V}_g$ in the model, whereas $\boldsymbol{Q}$ remains the same as in [33]. The second term $2\boldsymbol{\Theta}(k)^T \boldsymbol{U}(k)$ of the new CF in (18) is also a 1×1 vector, therefore

$$2\boldsymbol{\Theta}^T(k)\boldsymbol{U}(k) = 2\big[\boldsymbol{\Theta}^T(k)\boldsymbol{U}(k)\big]^T = 2\boldsymbol{U}(k)^T \boldsymbol{\Theta}(k). \tag{19}$$

Based on the above analysis, the following algebraic manipulation and grouping can be derived in (20), shown at bottom of next page, for the CF.

The constant term that consists of $\boldsymbol{Q}$, $\boldsymbol{\Theta}(k)$, and $\theta(k)$ is dependent on the current state $\boldsymbol{x}(k)$, switch sequence $\boldsymbol{u}(k-1)$, reference $\boldsymbol{Y}^*$, and grid voltage $\boldsymbol{V}_{\text{g}}$, which are known values

$$\begin{aligned} J &= J_A + J_B \\ &= \underbrace{\|\boldsymbol{\Gamma x}(k) - \boldsymbol{Y}^*(k)\|_2^2 + \|\boldsymbol{\Psi V}_g(k)\|_2^2 + \lambda_u \|\boldsymbol{EU}(k-1)\|_2^2 + 2[\boldsymbol{\Gamma x}(k) - \boldsymbol{Y}^*(k)]^T \boldsymbol{\Psi V}_g(k)}_{\theta(k)} + 2[\boldsymbol{\Gamma x}(k) - \boldsymbol{Y}^*(k)]^T [\boldsymbol{\Upsilon U}(k)] \\ &\quad + 2[\boldsymbol{\Upsilon U}(k)]^{\boldsymbol{T}} \boldsymbol{\Psi V}_g(k) - 2\lambda_u \Big\{[\boldsymbol{EU}(k-1)]^{\boldsymbol{T}} \boldsymbol{SU}(k)\Big\} + \boldsymbol{U}(k)^{\boldsymbol{T}} \big\{\boldsymbol{\Upsilon}^{\boldsymbol{T}} \boldsymbol{\Upsilon} + \lambda_u \boldsymbol{S}^{\boldsymbol{T}} \boldsymbol{S}\big\} \boldsymbol{U}(k) \\ &= \underbrace{\|\boldsymbol{\Gamma x}(k) - \boldsymbol{Y}^*(k)\|_2^2 + \|\boldsymbol{\Psi V}_g(k)\|_2^2 + \lambda_u \|\boldsymbol{EU}(k-1)\|_2^2 + 2[\boldsymbol{\Gamma x}(k) - \boldsymbol{Y}^*(k)]^T \boldsymbol{\Psi V}_g(k)}_{\theta(k)} \\ &\quad + 2\underbrace{\Big\{[\boldsymbol{\Gamma x}(k) - \boldsymbol{Y}^*(k)]^T \boldsymbol{\Upsilon} + \boldsymbol{V}_g(k)^{\boldsymbol{T}} \boldsymbol{\Psi}^{\boldsymbol{T}} \boldsymbol{\Upsilon} - 2\lambda_u [\boldsymbol{EU}(k-1)]^{\boldsymbol{T}} \boldsymbol{S}\Big\}}_{\boldsymbol{\Theta}(k)} \boldsymbol{U}(k) + \boldsymbol{U}(k)^{\boldsymbol{T}} \underbrace{\big\{\boldsymbol{\Upsilon}^{\boldsymbol{T}} \boldsymbol{\Upsilon} + \lambda_u \boldsymbol{S}^{\boldsymbol{T}} \boldsymbol{S}\big\}}_{\boldsymbol{Q}} \boldsymbol{U}(k) \end{aligned} \tag{15}$$

that remain constant during the search. The constant term is not dependent on $\boldsymbol{U}$, which changes as each of the available solution sequences are investigated for optimality. For these reasons, the constant term may be omitted from the minimization problem. The rest term of the CF is, however, a function of the variable $\boldsymbol{U}$; this is the part that needs minimization. $\boldsymbol{Q}$ is a positive semidefinite matrix as $\boldsymbol{z}^{\mathrm{T}}\boldsymbol{Q}z > 0$ for all $\boldsymbol{z} \in \mathbb{R}, \boldsymbol{z}$ is a vector that belongs to $\mathbb{R}$. The transformation matrix $\boldsymbol{H}$ is a lower triangular matrix obtained by taking the Chelsey decomposition of $\boldsymbol{Q}^{-1}$

$$\boldsymbol{Q} = \boldsymbol{H}^{\boldsymbol{T}}\boldsymbol{H} \tag{21}$$

where $\boldsymbol{H}$ is a lower triangular matrix of $4N \times 4N$, which can be written as

$$\boldsymbol{H} = \begin{bmatrix} h_{11} & 0 & 0 \\ h_{21} & h_{22} & 0 \\ h_{31} & h_{32} & h_{33} \end{bmatrix}.$$

$\boldsymbol{H}$ remains the same after the inclusion of the grid voltage because $\boldsymbol{Q}$ remains unchanged with regard to [33]. The unconstrained optimum $\boldsymbol{U}_{\boldsymbol{unc}}$ is the optimal solution sequence obtained by removing the integer constraints of the switch state $\boldsymbol{u}$ as set out in (1), which is calculated as follows [33]:

$$\boldsymbol{U}_{\boldsymbol{unc}}(k) = -\boldsymbol{Q}^{-1}\boldsymbol{\Theta}(k). \tag{22}$$

Due to the changed $\boldsymbol{\Theta}(k)$, the unconstrained optimum $\boldsymbol{U}_{\boldsymbol{unc}}$ differs from that in [33] due to the influence of the grid. In the CF, $\boldsymbol{Q}$ and $\boldsymbol{Q}^{-1}(k)$ are now replaced by $\boldsymbol{H}^T\boldsymbol{H}$ and $\boldsymbol{U}_{\boldsymbol{unc}}$, respectively

$$\begin{aligned} J &= [\boldsymbol{U}(k) - \boldsymbol{U}_{\mathrm{unc}}(k)]^T \boldsymbol{H}^T\boldsymbol{H}[\boldsymbol{U}(k) - \boldsymbol{U}_{\mathrm{unc}}(k)] \\ &\quad + \mathrm{const}(k) \\ &= [\boldsymbol{H}(\boldsymbol{U}(k) - \boldsymbol{U}_{\mathrm{unc}}(k))]^T [\boldsymbol{H}\boldsymbol{U}(k) - \boldsymbol{H}\boldsymbol{U}_{\mathrm{unc}}(k)] \\ &\quad + \mathrm{const}(k) \\ &= \left[\boldsymbol{H}\boldsymbol{U}(k) - \bar{\boldsymbol{U}}_{\mathrm{unc}}(k)\right]^T \left[\boldsymbol{H}\boldsymbol{U}(k) - \boldsymbol{H}\bar{\boldsymbol{U}}_{\mathrm{unc}}(k)\right] \\ &\quad + \mathrm{const}(k) \end{aligned} \tag{23}$$

where $\bar{\boldsymbol{U}}_{\mathrm{unc}}(k)$ is a $4N \times 1$ column vector; the optimal switching sequence is achieved by searching the sequence that results in the minimum cost J in (23). This CF minimization problem is now reformulated into an ILS problem in vector form with $\boldsymbol{U}(k)$ as the optimal variable

$$\boldsymbol{U}_{\mathrm{opt}}(k) = \arg\min_{\boldsymbol{U}(k)} \boldsymbol{H}\boldsymbol{U}(k) - \bar{\boldsymbol{U}}_{\mathrm{unc}}(k)_2^2. \tag{24}$$

$\bar{\boldsymbol{U}}_{\mathrm{unc}}(k)$ is obtained by multiplying the unconstrained solution $\boldsymbol{U}_{\boldsymbol{unc}}(k)$ with the transformation matrix $\boldsymbol{H}$ given by

$$\bar{\boldsymbol{U}}_{\mathrm{unc}}(k) = \boldsymbol{H}\boldsymbol{U}_{\mathrm{unc}}(k). \tag{25}$$

In a system with p phases and each phase with s possible switching positions, the number of possible states $\boldsymbol{u}(k)$ can be calculated as s^p. In this article, we have 2^4 (16) possible switching states for the four-leg converter. The number of candidate switching sequences $\boldsymbol{U}(k)$ that exist over a horizon of N steps is s^{pN}. For a three-phase two-level four-leg system with two possible switching positions per phase, there are a total of 2^{4N} candidate switch sequences. As a result, the search for an optimal sequence lies within the set of all candidate sequences, each sequence is evaluated by the CF to find the least costly one. This approach is only feasible for short horizons because as the prediction step increases, the number of candidate solutions increases exponentially. In the case of long horizons, to alleviate the calculation load on the microprocessor, a sphere decoding algorithm can be used to optimize the search process.

B. Sphere Decoding With Babai Estimation

Sphere decoding is a maximum-likelihood detection method widely used in signal detection. By setting a hypersphere centered on the receiving vector, just the lattice points in the hypersphere are searched to find the maximum-likelihood solution, thus complicated search is avoided. In a tree search with the sphere decoding algorithm, there are two search strategies, namely the Fincke–Phost (FP) strategy [35] and the Schnorr–Euchner (ER) strategy [36], both are adopted in this article. The aim of sphere decoding is to exclude as many suboptimal solutions as possible from the search tree by only evaluating solution points within a radius ρ of a sphere centered around the transformed unconstrained optimum vector $\bar{\boldsymbol{U}}_{\boldsymbol{unc}}$

$$\rho(k) = \bar{\boldsymbol{U}}_{\mathrm{unc}}(k) - \boldsymbol{H}\boldsymbol{U}(k)_2. \tag{26}$$

Here, $\boldsymbol{U}(k)$ is a $4N \times 1$ column vector where each element can only be either 1 or –1, two possible cases. This means $\boldsymbol{U}(k)$ has 2^{4N} cases, each case corresponds to a CF J, whereas $\boldsymbol{H}$ is a $4\mathrm{N} \times 4\mathrm{N}$ lower triangular matrix. Then, the CF can be expressed as in [37]

$$\begin{aligned} J &= (\bar{u}_{\mathrm{unc1}} - h_{11}u_1)^2 + (\bar{u}_{\mathrm{unc2}} - h_{21}u_1 - h_{22}u_2)^2 \\ &\quad + (\bar{u}_{\mathrm{unc3}} - h_{31}u_1 - h_{32}u_2 - h_{33}u_3)^2 + \cdots. \end{aligned} \tag{27}$$

$$\begin{aligned} J &= \|\boldsymbol{U}(k)\|_{\boldsymbol{Q}}^2 + 2\boldsymbol{\Theta}^T(k)\boldsymbol{U}(k) + \theta(k) \\ &= \boldsymbol{U}^T(k)\boldsymbol{Q}\boldsymbol{U}(k) + \left[\boldsymbol{\Theta}^T(k)\boldsymbol{U}(k) + \boldsymbol{U}^T(k)\boldsymbol{\Theta}(k)\right] + \left[\boldsymbol{\Theta}^T(k)\boldsymbol{Q}^{-T}\boldsymbol{\Theta}(k) - \boldsymbol{\Theta}^T(k)\boldsymbol{Q}^{-T}\boldsymbol{\Theta}(k)\right] + \theta(k) \\ &= \left[\boldsymbol{U}^T(k)\boldsymbol{Q}\boldsymbol{U}(k) + \boldsymbol{U}^T(k)\boldsymbol{Q}\boldsymbol{Q}^{-1}\boldsymbol{\Theta}(k) + \boldsymbol{\Theta}^T(k)\boldsymbol{Q}^{-T}\boldsymbol{Q}\boldsymbol{U}(k) + \boldsymbol{\Theta}^T(k)\boldsymbol{Q}^{-T}\boldsymbol{Q}\boldsymbol{Q}^{-1}\boldsymbol{\Theta}(k)\right] - \boldsymbol{\Theta}^T(k)\boldsymbol{Q}^{-T}\boldsymbol{\Theta}(k) + \theta(k) \\ &= \left[\boldsymbol{U}(k) + \boldsymbol{Q}^{-1}\boldsymbol{\Theta}(k)\right]^T\boldsymbol{Q}\left[\boldsymbol{U}(k) + \boldsymbol{Q}^{-1}\boldsymbol{\Theta}(k)\right] - \boldsymbol{\Theta}^T(k)\boldsymbol{Q}^{-T}\boldsymbol{\Theta}(k) + \theta(k) \\ &= \left[\boldsymbol{U}(k) + \boldsymbol{Q}^{-1}\boldsymbol{\Theta}(k)\right]^T\boldsymbol{Q}\left[\boldsymbol{U}(k) + \boldsymbol{Q}^{-1}\boldsymbol{\Theta}(k)\right] + \mathrm{const}(k) \end{aligned} \tag{20}$$

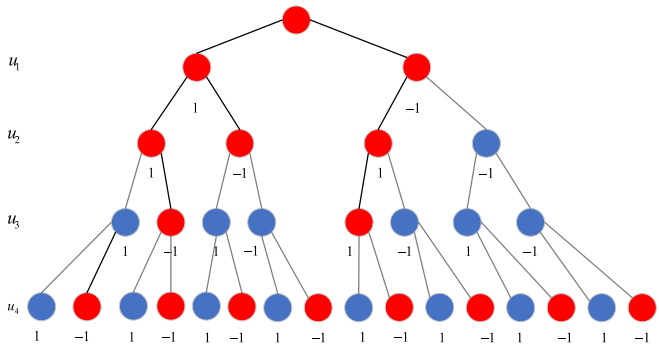

Fig. 2. Tree search structure of sphere decoding algorithm.

TABLE I
IMPLEMENTATION OF SPHERE DECODING BASED ON BABAI ESTIMATION

Algorithm 1 sphere decoding

Function $U_{opt}, \rho^2 = SphDec(U, d^2, i, \rho^2, \overline{U}_{unc})$
  for each $u\epsilon\{-1,1\}$ **do**
    $U_i = u$
    $d^{'2} = \left\|\overline{U}_{i,unc}(k) - H_{i,1:i}U_{1:i}\right\|^2 + d^2$
  if $d^{'2} \le \rho^2$ **then**
    if $i < 4N$ **then**
      $U'_{opt}, \rho^{'2} = SphDec\left(U, d^{'2}, i+1, \rho^2, \overline{U}_{unc}\right)$
      $U_{opt} = U'_{opt}$
      $\rho^2 = \rho^{'2}$
  else
    $U_{opt} = U$
    $\rho^2 = d^{'2}$
  end if
end if
end for end function

The CF is the sum of $4N$ square terms. As every element of $\boldsymbol{U}(k)$, $u_i(i = 1,\ldots,4N)$, can only be –1 or 1, the CF can be expressed in the form of a binary tree, as shown in Fig. 2.

In Fig. 2, the principle of sphere decoding is illustrated using a four-layer binary tree. Each line segment embodies one of the square terms of the CF. So, the sum of the length line from the root node to the bottom leaf node is the value of the CF. An exhaustive search can calculate and compare the CFs for each case, but this would take a lot of computational time. Sphere decoding first set an initial radius d_0, thereafter it calculates from left to right, layer by layer, to determine whether the sum of the accumulated radius squares are less than the initial radius squared d_0^2. The red dots represent the available paths, whereas the blue dots show those not adopted. When $(u_1, u_2, u_3, u_4) = (1,\ 1,\ 1, 1)$, the sum of the accumulated radius is larger than the initial radius and is not selected. When $(u_1, u_2, u_3, u_4) = (1,\ 1,\ -1, 1)$, the sum of the accumulated radius is less than the initial radius. The initial radius updates this accumulated radius and returns to the previous layer to continue the above operation. The best switching sequence $\boldsymbol{U}(k)$ is $(u_1, u_2, u_3, u_4) = (-1,\ 1,\ 1, 1)$. Table I shows the implementation steps of this task based on the aforementioned explanations using the Babai estimate method.

TABLE II
IMPLEMENTATION OF SPHERE DECODING BASED ON NODE COMPARISON METHOD

Algorithm 2: node comparison method

Function $U_{opt}, \rho^2 = SphDec(U, d^2, i, \rho^2, \overline{U}_{unc})$
  for each $u\epsilon\{-1,1\}$ **do**
    $U_i = u$
  $\bar{d}_1 = \|\bar{u}_{unc1} - h_{11}\|^2,\ \ \bar{d}_2 = \|\bar{u}_{unc2} + h_{11}\|^2$
  $\bar{d}_1 = \min(\bar{d}1, \bar{d}_2)$
if $\bar{d}_1 \le \bar{d}_2$ **then**
  $u_{i-1} = 1$
else
  $u_{i-1} = -1$
end if
  $\bar{d}_1 = \left\|\bar{u}_{unci} - h_{i,1:(i-1)}u_{1:(i-1)} - h_{ii}\right\|^2$
  $\bar{d}_2 = \left\|\bar{u}_{unci} - h_{i,1:(i-1)}u_{1:(i-1)} + h_{ii}\right\|^2$
  $d_2 = \min(\bar{d}_1, \bar{d}_2)$
  $d_1 = d_1 + d_2$
while $(i < 4N)$
end for end function

It should be noted that the initial radius d_0 plays a significant role in reducing the computational expense of sphere decoding. It cannot be so small that the optimal solution may be obliterated.

C. Sphere Decoding Using the Node Comparison Method

To further optimize the initial radius selection, in this article, a novel node comparison method is adopted to estimate the initial radius d_0, and its implementation is shown in Table II. The idea behind the node comparison method is as follows: compare the length of two paths corresponding to each node of the search tree, take the branch with smaller results, go on and compare the length of two paths of the branch nodes, and so on, then superposition the path length. The final length of the total path is set as the initial radius. The node comparison method itself produces a suboptimal solution (or optimal solution), so the initial radius cannot be so small that sphere decoding will exclude the real optimal solution. Compared with Babai estimation, the computational load from the node comparison method can be reduced further.

Set the optimal solution as $\boldsymbol{U}_{\rm opt}(k)$, then it should satisfy

$$\boldsymbol{U}_{\rm opt}\ (k) = \arg\min_{\boldsymbol{U}(k)} \bar{\boldsymbol{U}}_{\rm unc}\ (k) - \boldsymbol{H}\boldsymbol{U}(k)^2. \qquad (28)$$

When the initial radius $\rho_{\rm ini}(k)$ of each sampling time is determined by the node comparison method, the searching algorithm in Table II is performed according to the principle of sphere decoding.

Based on the above analysis, an FC-MPC of a three-phase four-leg *LCL*-GCC can be realized. A block diagram of the proposed FC-MPC with sphere decoding is shown in Fig. 3.

D. Implementation of the Proposed Method

Fig. 4 shows the flowchart that explains the implementation procedure of the proposed method. The first task is to initialize some parameters, such as the *LCL*-filter parameters, and provide

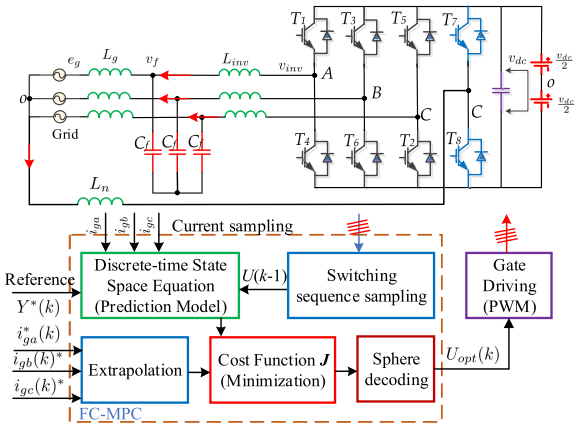

Fig. 3. FC-MPC control for three-phase two-level *LCL*-type four-leg GCCs with sphere decoding.

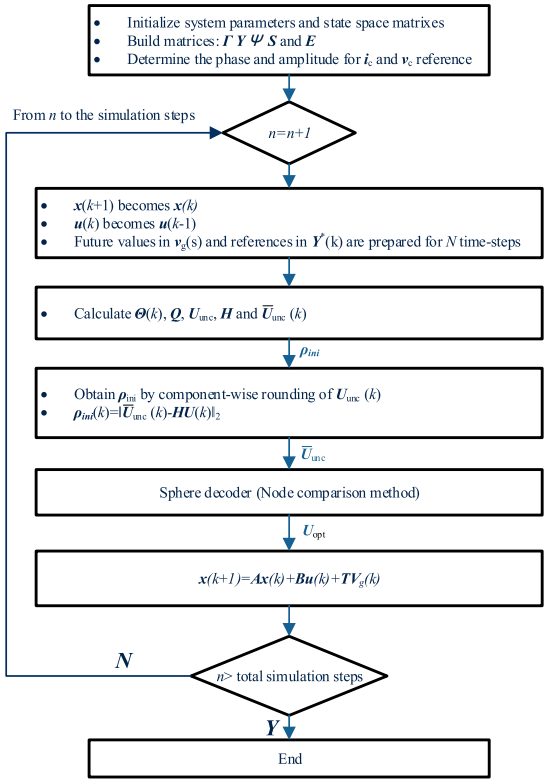

Fig. 4. Implementation flowchart of the FC-MPC method with sphere decoding.

the state-space equation that describes the behavior of the GCC. These parameters will be used to build the integral formulation matrices, namely $\boldsymbol{\Gamma}, \boldsymbol{\Upsilon}, \boldsymbol{\Psi}, \boldsymbol{S}$,and $\boldsymbol{E}$. The phase and amplitude reference for $\boldsymbol{i}_1$ and $\boldsymbol{v_c}$ are determined by phase calculation with the given grid-current reference.

During each simulation step, the optimization and sphere decoder are applied to select the optimal switching sequence and apply its first switching vector before the next re-evaluation. The future state value of the system $\boldsymbol{x}(k+1)$ is calculated using the discrete-time equation in (6), then it becomes the current state. The future references in $\boldsymbol{Y}^*(k)$ for $\boldsymbol{i}_1$, $\boldsymbol{i}_2$, and $\boldsymbol{v_c}$ are prepared for

TABLE III
PARAMETER SPECIFICATION FOR SIMULATION

Parameters	Symbol	Value
DC voltage	V_{DC}	1000 V
The grid voltage (RMS)	V_g	$220\sqrt{2}$ V
Reference of the grid-side current	I_2^*	20 A
Inverter-side inductance	L_1	20 mH
Grid side inductance	L_2	1.6 mH
Neutral-leg inductance	L_n	1.6 mH
Inverter-side resistance	R_1	0.1 Ω
Grid-side resistance	R_2	0.1 Ω
Filter capacitance	C	65 μF
Resonance damping resistance	R_c	5 Ω
Sampling time	T_s	20 μs

N time steps of the horizon. The grid voltage $\boldsymbol{V}_g(k)$ can also be filled with its N future values. Thereafter, $\boldsymbol{\Theta}(k)$, $\boldsymbol{Q}$, $\boldsymbol{U_{unc}}(k)$, $\boldsymbol{H}$, and the transformed unconstrained solution $\bar{\boldsymbol{U}}_{\rm unc}(k)$ will be calculated. The initial radius $\boldsymbol{\rho}_{\rm ini}(k)$ is the Euclidean distance between the transformed initial solution estimate and the transformed unconstrained solution. $\boldsymbol{U_{unc}}(k)$and $\boldsymbol{\rho}_{\rm ini}(k)$ are then input to the sphere decoder function (using Babai estimate or node-comparison method) to achieve a fast search for the optimum sequence. The output of the sphere decoding function returns the optimal switching sequence $\boldsymbol{U_{opt}}(k)$. This loop continues until the all the simulation steps are finished.

IV. SIMULATIONS

To demonstrate the validity of the proposed method, a MATLAB/Simulink model was established for three-phase two-level four-leg GCCs. The parameter specifications are shown in Table III.

The constants in the C matrix of the state-space model are assigned to be $\lambda_1 = \lambda_2 = 1$ for the grid-side and inverter-side currents, and $\lambda_3 = 0.1$ for the filter-capacitor voltage. The weighting factor λ_u is applied as a penalty on the switching term in the CF. The switching frequency is calculated as an average by dividing half of the total switch changes throughout the steady state of the simulation. The controller searches for a new optimal sequence at every sampling instant.

In the following section, the parameter configuration, a performance evaluation of the GCCs chosen switching sequence, initial radius selection, steady-state and transient responses, and calculation expense comparisons between the proposed method and the traversing method in [10] and [11] will be given.

A. *Influence of Weight Factor* λ_u

To illustrate the influence of weight factor λ_u on the steady-state performance of the system, first the grid current reference $i_{\rm gref} = 20$ A and predictive horizon $N = 4$ are selected. In Fig. 5, the relationship between λ_u and the THD of the grid current, the tracking error, as well as the switching frequency is shown. As λ_u increases, the switching power losses have greater weight in the CF. Thus, reducing the switching frequency will increase the THD and tracking error. Also, as shown in Fig. 5(c), λ_u has little influence on switching loss reduction when $\lambda_u < 10^{-2}$. However, it can balance the switching losses and power

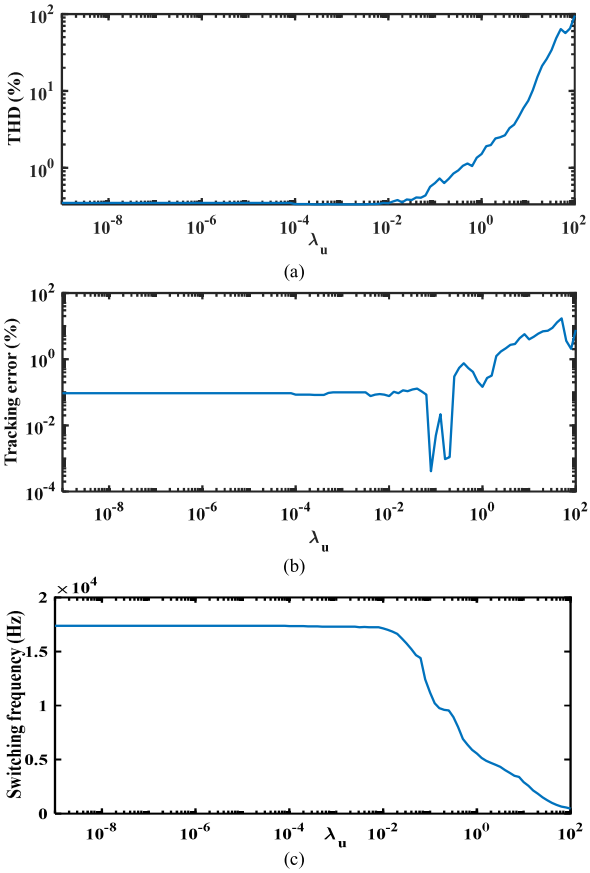

Fig. 5. THD, grid current tracking error, and switching frequency with the changes of weight factor $\boldsymbol{\lambda_u}$. (a) THD of the grid current. (b) Tracking error of the grid current. (c) Switching frequency of the power transistors.

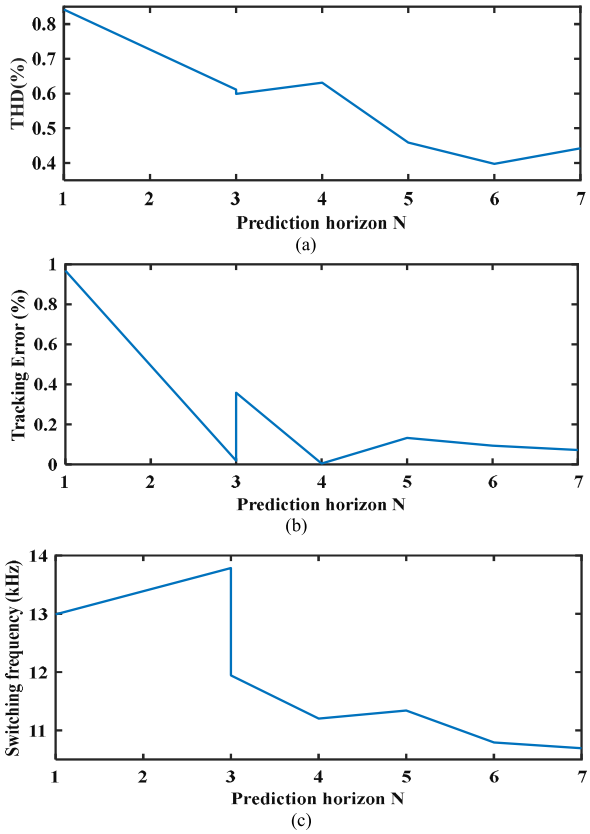

Fig. 6. THD, grid current tracking error, and switching frequency changes according to the size of the prediction horizon $\boldsymbol{N}$. (a) THD of the grid current, (b) tracking error of the grid current, and (c) switching frequency of the power transistors.

quality of the grid current when $10^{-2} \leq \lambda_u \leq 1$. As a result, $\lambda_u = 0.1$ was selected.

B. Influence of Predictive Horizon

To illustrate the performance of predictive horizon N on THD, tracking error, and switching frequency performance of the system, the grid current reference $i_{\text{gref}} = 20$ A and the weight factor $\lambda_{\text{u}} = 0.1$ are applied. The results in Fig. 6 (a)–(c) shows that with the increase in N (from 1 to 7), THD of the grid current decreases from 0.85% to 0.4%, the tracking error fluctuates from 0.95% to 0.1, and the switching frequency decreases from 13.8 to 10.8 kHz.

C. Initial Radius Selection

Fig. 7 shows the initial radius selection comparison results for node comparison and Babai estimation methods during the search for the optimal switching sequence using sphere decoding. At $\lambda_u = 0.1$ and $N = 4$, the average initial radius for the node comparison method is around 2.5 and around 5 for the Babai estimation method. We can see that the initial radius of the node comparison method is much smaller. Thus, we can say that the node comparison method eliminates more suboptimal solutions and reduces computational expense. Compared with

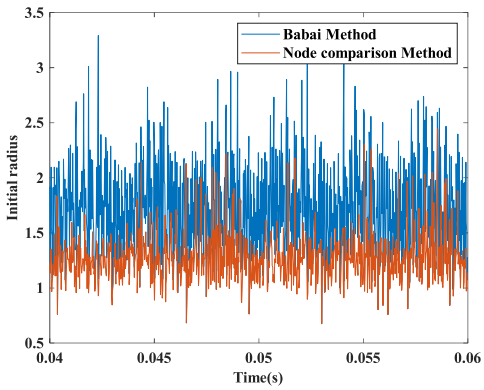

Fig. 7. Initial radius selection comparisons of sphere decoding algorithm with node comparison and Babai estimation.

Babai estimation, the implementation time with the proposed node comparison method is reduced by 37.23%.

D. Steady-State Analysis

To examine the steady-state behavior, $i_{\text{gref}} = 20$ A, $\lambda_u = 0.1$, and $N = 4$ are selected. Fig. 8(a) shows the steady-state response and the harmonic spectrum of the grid current under a balanced grid voltage where the tracking error is 0.093464%. As shown in Fig. 7(b), the THD of the grid-connected current

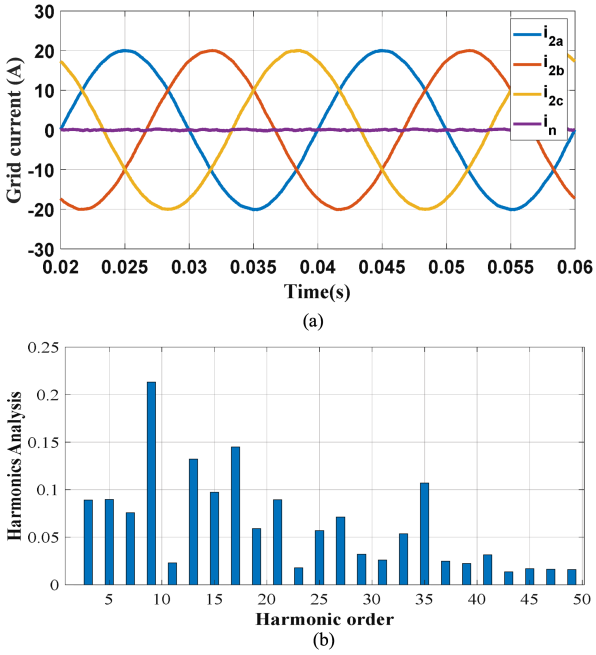

Fig. 8. Grid-side current and its harmonics. (a) Response time of the three-phase grid current in a steady state. (b) Harmonic spectrum.

is 0.39725%. These results demonstrate that the proposed FC-MPC method with the designed CF has excellent performance while the power quality of the grid current meets the IEEE- 1574 standard [4].

E. Transient Analysis

To verify the dynamic performance of the proposed FC-MPC control method with sphere decoding, the weight factor $\lambda_u = 0.1$ and prediction horizon $N = 4$ are applied. Fig. 8 shows the dynamic response of the grid current when the reference current changes. As shown in Fig. 9(a), when the step-down grid current reference changes from 20 to 5 A at 0.026 s, the response time is less than 3 ms. Similarly, as shown in Fig. 9(b), when a step-up grid current reference from 5 to 20 A is given, the grid current can be well tracked within 3 ms. These results show that the proposed method can keep good dynamic tracking performance over large current variations with only a small overshoot and excellent response times. Fig. 9(c) and (d) shows the grid current and neutral line current when a step-up and a step-down current references are given; the results show that for balance loads, the neutral-line current will always be zero during the transient time.

In some cases, it is required that different grid currents for each phase are provided, four-leg GCCs have the clear advantage in this case. Fig. 9(e) shows the response time of the grid current under an unbalanced grid current reference, the results show that neutral-line current can flow to the fourth leg of the converter. The grid current for each phase can be controlled independently.

F. Calculation Expense Analysis

Considering that calculation expense increases with the increase of prediction horizon, the number of floating-point

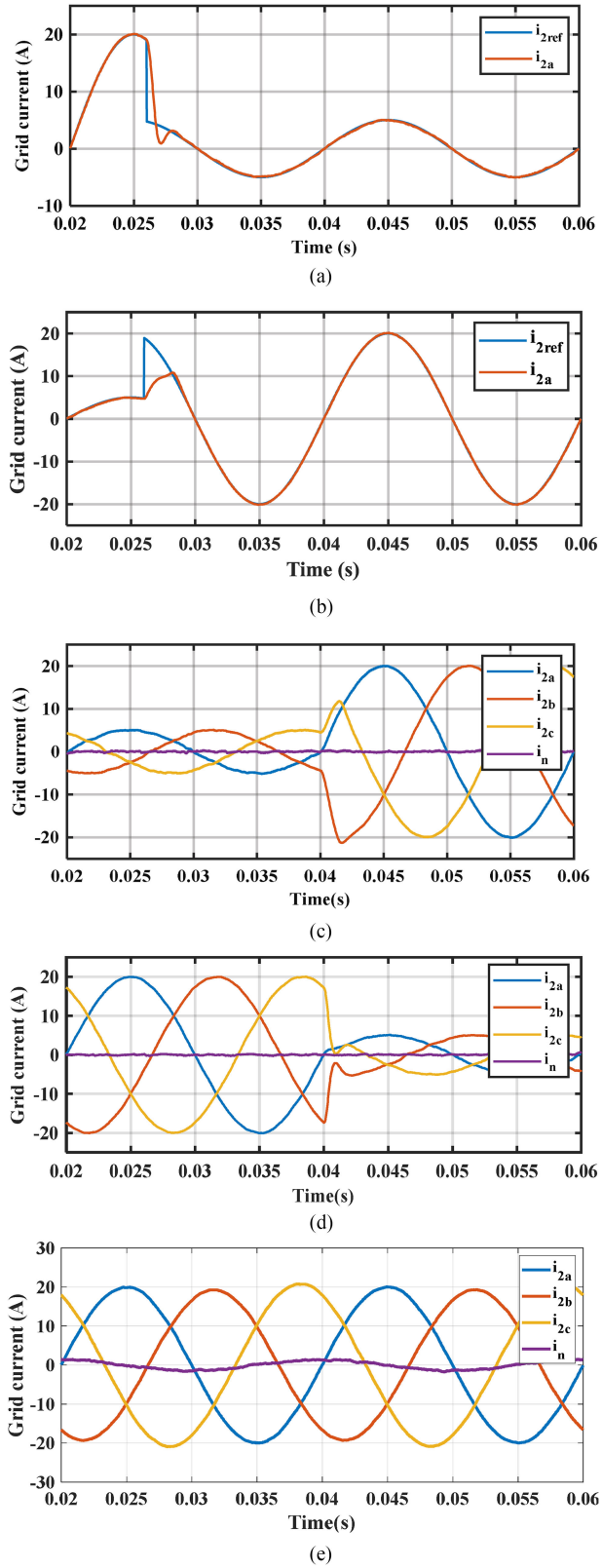

Fig. 9. Dynamic response of the grid current under balanced and unbalanced grid current references. (a) Response time of a step-down grid-side current and reference. (b) Response time of the grid current when a step-up reference is given. (c) Response time of the three-phase and neutral-phase currents when a step-up reference is given. (d) Response time of the three-phase and neutral-phase currents when a step-down reference is given. (e) Response time of the three-phase and neutral-phase currents under unbalanced grid current reference.

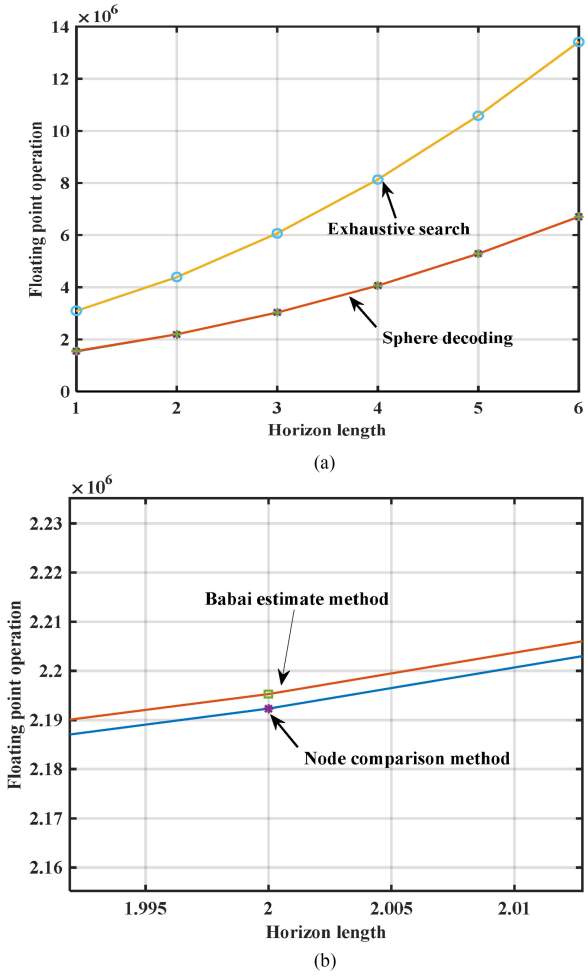

Fig. 10. FLOPS according to different search tree methods. (a) FLOPS with and without sphere decoding. (b) FLOPS with Babai estimation and node comparison method ($N = 2$).

operations (FLOPS) performed during the execution of the solution search with a prediction horizon N ranging from 1 to 6 was calculated. In the simulation, 1000 sampling points are used within each period.

When counting FLOPS, subtraction, multiplication, division, and the square root operation each count as one FLOP. An exhaustive search was performed by modifying the sphere decoding function in a way so it does not prune suboptimal solution branches and explores the whole search tree. This sphere decoding differs with the conventional traversing method in [10] and [11] by performing an exhaustive search to get the possible control sequence through a systematic exploration of the search tree, and so offers simplified adaptation of the prediction horizon.

Fig. 10(a) shows the computational efficiency that the sphere decoding algorithm offers by counting the FLOPS. In [10] and [11], the exhaustive search tree method is used. It can be clearly seen from Fig. 10(a), without sphere decoding, an overwhelming amount of calculations must be performed while traversing the tree to minimize the CF. Obviously, this calculation expense can be greatly reduced with the sphere decoding method.

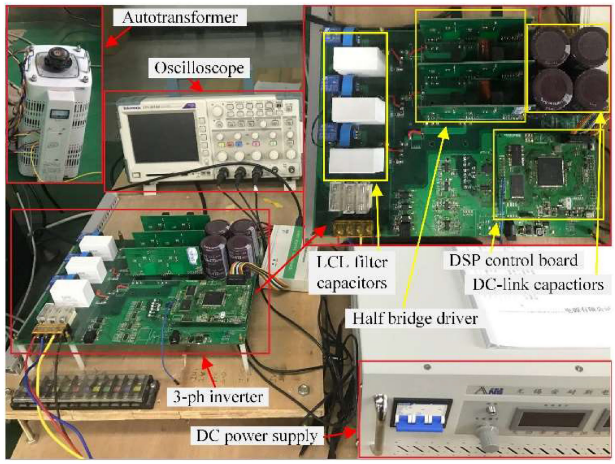

Fig. 11. Block diagram of experimental setup and designed *LCL*-type GCCs.

TABLE IV
PARAMETER SPECIFICATION FOR EXPERIMENT

Symbol	Parameter	Values
P_e	Rated power	10 kW
V_{dc}	DC-link voltage	700 V
e_g	Grid voltage (RMS)	220 Vac
f_g	Grid frequency	50 Hz
C_{dc}	DC-link capacitance	3 mF
L_1	Output filter inductance	2 mH
L_g	Output filter inductance	1 mH
C_f	Filter capacitance	2.2 μF
N	Prediction horizon	4
λ_u	Weight factor for switching frequency	0.1
r	Equivalent resistor of output filter inductance	0.26 Ω

Fig. 10(b) shows a FLOPS comparison between Babai estimation and the node comparison method when the prediction horizon $N = 2$. The results show that the number of FLOPS used by the Baibai estimation method can be further reduced by using the proposed node comparison method. This demonstrates that the proposed method is superior to the Babai method in terms of initial radius selection, which further alleviates the calculation expense.

V. EXPERIMENTS

A. Hardware Setup

To validate the performance of the proposed FC-MPC control method for four-leg GCCs, a hardware prototype of a 10-kVA three-phase four-leg two-level GCC was setup in the laboratory. Fig. 11 shows the hardware configuration and the designed *LCL*-type four-leg GCC. Table IV shows the nominal experimental parameters.

The control scheme in Fig. 4 was implemented with a 32-b float-point digital signal processor TMS320F28335 from Texas Instruments, which is usually used for fast complicated mathematics calculations and control algorithm implementation. The four-leg power converter is composed of eight power transistors with the IMZ120R045M1 from Infineon. All the power MOSFETs are driven by the isolation driver 1ED20I12FA2. Six Hall current

sensors (HCS-LTS-06A) are used for inverter-side current and grid-side current measurements.

For grid and filter capacitor voltage sampling, a high precision series voltage divider and a full differential isolation amplifier ACPL-C790 with 0.5% high gain accuracy, 0.05% excellent linearity, and 200-kHz wide bandwidth were used. Since the output voltage ranges from –1.5 to 1.5 V, a forward-bias voltage circuit with a single-supply and rail-to-rail operational amplifier OPA4340 was used to convert –1.5 to 1.5 V into 0–3 V; this allows the system to connect with the ADC port of the microprocessor.

A four-channel Tektronix Oscilloscope TDS2010B was used for voltage and current measurements. The waveforms were recorded during steady states and transient states with a balanced grid. The four-leg GCC with an *LCL* output filter was connected to the grid through a variable three-phase transformer. The power circuit of the hardware configuration is the same as that in Fig. 3.

Verification of the proposed scheme includes looking at the steady-state and transient responses of the grid-side current both in *dq* and *abc* coordinates. The current tracking performance was also examined under sampling time variations.

B. Results and Analysis

1) Steady-State Analysis: To realize high power factor control, a grid current reference under the *dq* frame was given. Fig. 12(a) and (b) presents the experimental results of the grid current under *dq* coordinates. The grid current references under the *dq* frame are given as $i_d^* = 8$ A and $i_q^* = 0$ A. The sampling time T_s was set to both 200 and 100 μs during tests. It is possible to observe the convergence of i_{dq} to its reference. The performance of the systems with $T_s = 200$ μs and $T_s = 100$ μs were very similar.

In some cases, reactive power compensation is needed, therefore grid current references when $i_d^* > 0$ and $i_q^* < 0$ are given. Fig. 12(c) and (d) presents the experimental results of the active and reactive grid currents with references $i_d^* = 6$ A and $i_q^* = -5$ A and a sampling time T_s of 200 or 100 μs. The results show that the grid current phase leads the grid voltage by 90°, as such reactive power compensation can be realized. Even at a low sampling frequency, high-accuracy grid-side current tracking control can be achieved.

The steady-state results show that power quality of the grid current is pretty good. When the power factor is 1, the grid voltage and current are in phase. When the GCCs operate in the reactive power compensation mode, there is a phase lag between the grid current and grid voltage. In addition, the distortion of the grid current increases when the sampling time decreases.

2) Transient Analysis: To demonstrate the dynamic behavior of the proposed method, following cases are examined.

Case 1: In the beginning, the grid current references under *dq* coordinates with $i_d^* = 4$ A and $i_q^* = 0$ A are given. When they reach a steady state, the reference currents are changed to $i_d^* = 8$ A and $i_q^* = 0$ A, a sampling time T_s of 100 μs was used. Fig. 13(a) shows the phase voltage and grid-side current in phase-A. Fig. 13(b) shows the grid-side current of phase-A under *dq* coordinates.

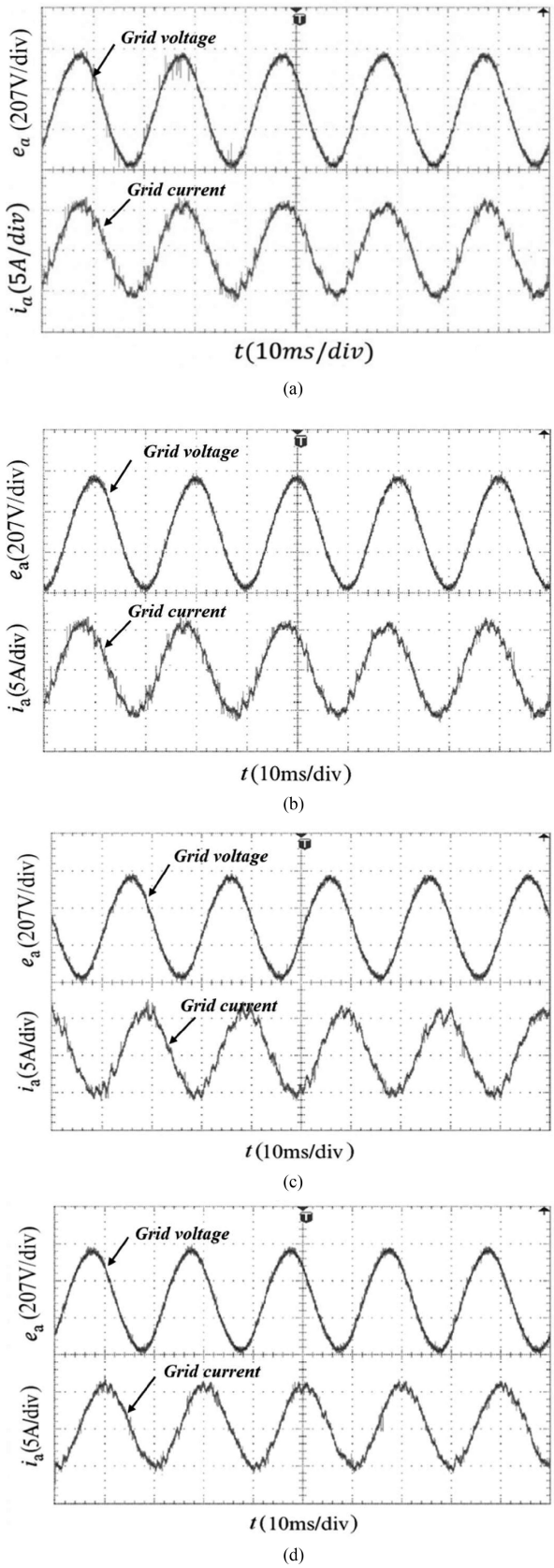

Fig. 12. Unity power factor and reactive power compensation control. (a) $i_d^* = 8$ A, $i_q^* = 0$ A, *and* $T_s = 200$ μs. (b) $i_d^* = 8$ A, $i_q^* = 0$ A, *and* $T_s = 100$ μs. (c) $i_d^* = 6$ A, $i_q^* = -5$ A, *and* $T_s = 200$ μs. (d) $i_d^* = 6$ *A*, $i_q^* = -5$ A, *and* $T_s = 100$ μs.

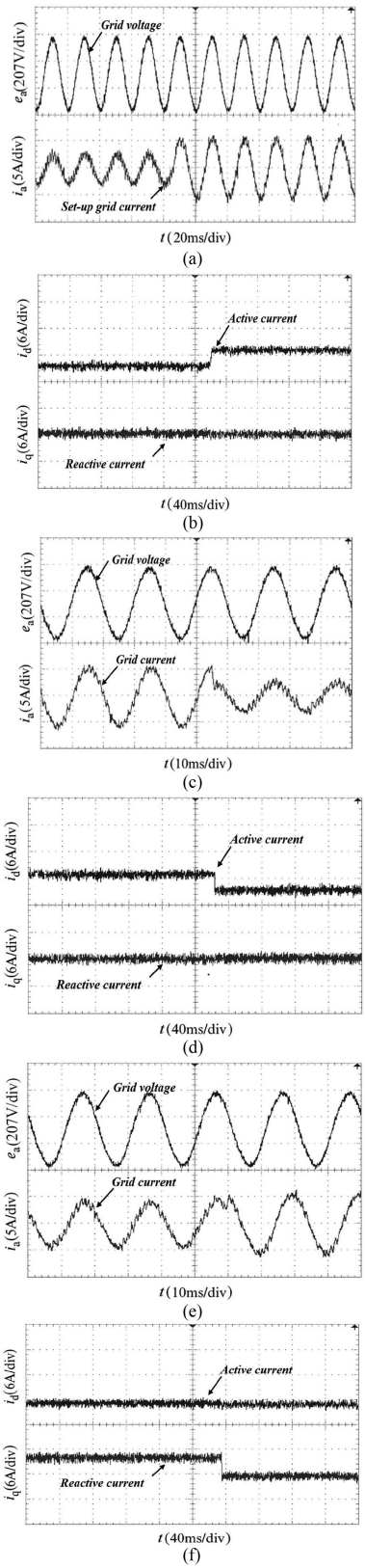

Fig. 13. Transient response of grid-side current in different cases. (a) Step-up grid current reference (Case 1). (b) Grid-current under *dq* coordinates (Case 1). (c) Step-down grid current reference (Case 2). (d) Grid-current under *dq* coordinates (Case 2). (e) Phase voltage and current of phase-A (Case 3). (f) Active and reactive grid currents (Case 3).

Case 2: In the beginning, the grid-side current references with $i_d^* = 8$ A and $i_q^* = 0$ A are given. When the system enters a steady state, the current references are changed to $i_d^* = 4$ A and $i_q^* = 0$ A by the personal computer using controller area network communication. The sampling time used was $T_s = 100\mu$s. Fig. 13(c) shows the phase voltage and current of phase-A. Fig. 13(d) shows the grid-side current of phase-A under *dq* coordinates.

Case 3: In the beginning, the grid current references with $i_d^* = 6$ A and $i_q^* = 0$ A are given. As long as the system is in a steady state, the active current component i_d^* remains unchanged while the reactive current i_q^* changes from 0 to -5 A. The sampling time used was $T_s = 100\mu$s. Fig. 13(e) shows that the phase voltage e_a and current i_a are in phase before new i_q^* is applied. The reactive current i_q again follows its reference within 2 ms. Fig. 13(f) shows the transient response of i_d and i_q when a step-down reactive current reference i_q^* is given.

From the steady and transient responses of the grid current, as shown in Figs. 12 and 13, the system proves that it has pretty good steady-state and dynamic behavior. When the grid current references under *dq* coordinates are changed, the feedback grid current obtains good convergence of the i_{dq} to its reference i_{dq}^*. In addition, the experimental results also show that the active and reactive grid-side current components can be controlled independently.

VI. Conclusion

This article investigated two novel sphere decoding algorithms that can greatly reduce the calculation load required to find optimal control solutions during CF minimization for FC-MPC-controlled four-leg GCCs. The proposed method was realized by transforming the optimization of the MPC CF into an ILS problem. The search time for an optimal control sequence was greatly reduced by reducing the associated computational cost. Furthermore, the Babai estimation and node comparison methods, which are used for initial radius selection during sphere decoding, were proposed. Both methods offer a significant reduction in FLOPS while searching for optimal control solutions. Case studies on four-leg GCCs were carried out to validate and compare the two proposed methods and demonstrate their effectiveness. The proposed method can be further extended and applied to other FC-MPC-controlled power converters.

References

[1] B. Long *et al.*, "Design and implementation of a virtual capacitor-based DC current suppression method for grid-connected inverters," *ISA Trans.*, vol. 92, pp. 257–272, 2019.

[2] B. Long, M. Zhang, Y. Liao, L. Huang, and K. T. Chong, "An overview of DC component generation, detection and suppression for grid-connected converter systems," *IEEE Access*, vol. 7, pp. 110426–110438, 2019.

[3] IEEE Recommended Practice for Utility Interface of Photovoltaic (PV) Systems, IEEE Std 929-2000, 2000.

[4] IEEE Standard for Interconnection and Interoperability of Distributed Energy Resources With Associated Electric Power Systems Interfaces, IEEE Std 1547-2018 (Revision of IEEE Std 1547-2003), 2018.

[5] IEEE Draft Standard Conformance Test Procedures for Equipment Interconnecting Distributed Energy Resources With Electric Power Systems and Associated Interfaces, IEEE P1547.1/D9.8, Dec. 2019.

[6] M. Lu, X. Wang, P. C. Loh, and F. Blaabjerg, "Resonance interaction of multiparallel grid-connected inverters with LCL filter," *IEEE Trans. Power Electron.*, vol. 32, no. 2, pp. 894–899, Feb. 2017.
[7] C. Yu *et al.*, "Modeling and resonance analysis of multiparallel inverters system under asynchronous carriers conditions," *IEEE Trans. Power Electron.*, vol. 32, no. 4, pp. 3192–3205, Apr. 2017.
[8] S. Leitner, M. Yazdanian, S. Ziaeinejad, A. Mehrizi-Sani, and A. Muetze, "Internal model-based active resonance damping current control of a grid-connected voltage-sourced converter with an LCL filter," *IEEE Trans. Power Syst.*, vol. 33, no. 6, pp. 6025–6036, Nov. 2018.
[9] X. Guo, D. Xu, and B. Wu, "Four-leg current-source inverter with a new space vector modulation for common-mode voltage suppression," *IEEE Trans. Ind. Electron.*, vol. 62, no. 10, pp. 6003–6007, Oct. 2015.
[10] V. Yaramasu, M. Rivera, B. Wu, and J. Rodriguez, "model predictive current control of two-level four-leg inverters—Part I: Concept, algorithm, and simulation analysis," *IEEE Trans. Power Electron.*, vol. 28, no. 7, pp. 3459–3468, Jul. 2013.
[11] M. Rivera, V. Yaramasu, J. Rodriguez, and B. Wu, "model predictive current control of two-level four-leg inverters—Part II: Experimental implementation and validation," *IEEE Trans. Power Electron.*, vol. 28, no. 7, pp. 3469–3478, Jul. 2013.
[12] M. Pichan and H. Rastegar, "Sliding-mode control of four-leg inverter with fixed switching frequency for uninterruptible power supply applications," *IEEE Trans. Ind. Electron.*, vol. 64, no. 8, pp. 6805–6814, Aug. 2017.
[13] Y. He, X. Wang, X. Ruan, D. Pan, X. Xu, and F. Liu, "Capacitor-current proportional-integral positive feedback active damping for LCL-type grid-connected inverter to achieve high robustness against grid impedance variation," *IEEE Trans. Power Electron.*, vol. 34, no. 12, pp. 12423–12436, Dec. 2019.
[14] J. Rocabert, A. Luna, F. Blaabjerg, and P. Rodríguez, "Control of power converters in ac microgrids," *IEEE Trans. Power Electron.*, vol. 27, no. 11, pp. 4734–4749, Nov. 2012.
[15] B. Yang *et al.*, "Energy reshaping based passive fractional-order PID control design and implementation of a grid-connected PV inverter for MPPT using grouped grey wolf optimizer," *Sol. Energy*, vol. 170, pp. 31–46, 2018.
[16] Q. G. Xiao, Y. Yang, and Z. Zhang, "Advanced control of grid-connected current source converter under unbalanced grid voltage conditions," *IEEE Trans. Ind. Electron.*, vol. 65, no. 12, pp. 9225–9233, Dec. 2018.
[17] H. R. Baghaee, M. Mirsalim, G. B. Gharehpetian, and H. A. Talebi, "A generalized descriptor-system robust H∞ control of autonomous microgrids to improve small and large signal stability considering communication delays and load nonlinearities," *Int. J. Elect. Power Energy Syst.*, vol. 92, pp. 63–82, 2017.
[18] G. G. Koch, H. Pinheiro, L. A. Maccari, R. C. L. F. Oliveira, A. A. Ferreira, and V. F. Montagner, "Robust H∞ control for rejection of voltage disturbances in grid-connected converters," in *Proc. 12th IEEE Int. Conf. Ind. Appl.*, 2016, pp. 1–6.
[19] J. Hu, L. Shang, Y. He, and Z. Q. Zhu, "Direct active and reactive power regulation of grid-connected DC/AC converters using sliding mode control approach," *IEEE Trans. Power Electron.*, vol. 26, no. 1, pp. 210–222, Jan. 2011.
[20] J. Xia, Y. Guo, X. Zhang, J. Jatskevich, and N. Amiri, "Robust control strategy design for single-phase grid-connected converters under system perturbations," *IEEE Trans. Ind. Electron.*, vol. 66, no. 11, pp. 8892–8901, Nov. 2019.
[21] R. P. Vieira, L. T. Martins, J. R. Massing, and M. Stefanello, "Sliding mode controller in a multiloop framework for a grid-connected VSI with LCL filter," *IEEE Trans. Ind. Electron.*, vol. 65, no. 6, pp. 4714–4723, Jun. 2018.
[22] S. Li, M. Fairbank, C. Johnson, D. C. Wunsch, E. Alonso, and J. L. Proaño, "Artificial neural networks for control of a grid-connected rectifier/inverter under disturbance, dynamic and power converter switching conditions," *IEEE Trans. Neural Netw. Learn. Syst.*, vol. 25, no. 4, pp. 738–750, Apr. 2014.
[23] M. Narimani, W. Bin, V. Yaramasu, C. Zhongyuan, and N. R. Zargari, "Finite control-set model predictive control (FCS-MPC) of nested neutral point-clamped (NNPC) converter," *IEEE Trans. Power Electron.*, vol. 30, no. 12, pp. 7262–7269, Dec. 2015.
[24] S. Vazquez, J. Rodriguez, M. Rivera, L. G. Franquelo, and M. Norambuena, "Model predictive control for power converters and drives: Advances and trends," *IEEE Trans. Ind. Electron.*, vol. 64, no. 2, pp. 935–947, Feb. 2017.
[25] C. Bordons and C. Montero, "Basic principles of MPC for power converters: Bridging the gap between theory and practice," *IEEE Ind. Electron. Mag.*, vol. 9, no. 3, pp. 31–43, Sep. 2015.
[26] F. An, W. Song, B. Yu, and K. Yang, "Model predictive control with power self-balancing of the output parallel DAB DC–DC converters in power electronic traction transformer," *IEEE J. Emerg. Sel. Topics Power Electron.*, vol. 6, no. 4, pp. 1806–1818, Dec. 2018.
[27] B. S. Riar, J. Scoltock, and U. K. Madawala, "Model predictive direct slope control for power converters," *IEEE Trans. Power Electron.*, vol. 32, no. 3, pp. 2278–2289, Mar. 2017.
[28] I. M. B. Hassine, M. W. Naouar, and M. B. Najiba, "Extended model predictive-sliding mode control for three-phase grid connected converters," *IEEE Trans. Ind. Electron.*, vol. 64, no. 2, pp. 1341–1349, Jan. 2016.
[29] I. M.-B. Hassine, M. W. Naouar, and N. Mrabet-Bellaaj, "Model predictive-sliding mode control for three-phase grid-connected converters,"*IEEE Trans. Ind. Electron.*, vol. 64, no. 2, pp. 1341–1349, Feb. 2017.
[30] S. Bayhan, M. Trabelsi, H. Abu-Rub, and M. Malinowski, "Finite control set model predictive control for a quasi-z-source four-leg inverter under unbalanced load condition," *IEEE Trans. Ind. Electron.*, vol. 64, no. 4, pp. 2560–2569, Apr. 2017.
[31] Y. Guo, H. Gao, Q. Wu, H. Zhao, J. Østergaard, and M. Shahidehpour, "Enhanced voltage control of VSC-HVDC-connected offshore wind farms based on model predictive control," *IEEE Trans. Sustain. Energy*, vol. 9, no. 1, pp. 474–487, Jan. 2018.
[32] K. S. Alam, Md. P. Akter, D. Xiao, D. Zhang, and F. Rahman, "Lyapunov-based model predictive control of three-phase four-leg inverter with LC filter," in *Proc. IEEE Energy Convers. Congr. Expo. (ECCE)*, 2018.
[33] T. Geyer and D. E. Quevedo, "Multistep finite control set model predictive control for power electronics," *IEEE Trans. Power Electron.*, vol. 29, no. 12, pp. 6836–6846, Dec. 2014.
[34] S. Sternberg, "Dynamical systems," Courier Corporation, Chelmsford, MA, USA, 2010.
[35] D. Seethaler, H. Artes, and F. Hlawatsch, "Efficient near-ML detection for MIMO channels: The sphere-projection algorithm," *Proc. IEEE Global Telecommun. Conf.*, 2003, vol. 3, pp. 2089–2093.
[36] M. Karthikeyan and D. Saraswady, "Sphere decoding using threshold based Schnorr-Euchner enumeration in MIMO system," in *Proc. Int. Conf. Recent Trends Inf. Technol.*, 2014, pp. 1–4.
[37] T. Geyer and D. E. Quevedo, "Multistep direct model predictive control for power electronics—Part 2: Analysis," in *Proc. IEEE Energy Convers. Congr. Expo.*, 2013, pp. 1162–1169.

Bo Long (Senior Member, IEEE) received the B.S. degree in electrical engineering from Xi'an Petroleum University, Xi'an, China, in 2001, and the Ph.D. degree in electrical engineering from Xian Jiaotong University, Xi'an, China, in 2008.

In 2008, he joined the Department of Power Electronics, School of Mechatronics Engineering, University of Electronic Science and Technology of China (UESTC), Chengdu, China, where he was promoted to an Associate Professor in 2014. From 2017 to 2018, he was a Visiting Scholar (Guest Postdoctoral Researcher) in renewable energy and microgrids with the Department of Electrical Engineering, Tsinghua University, Beijing, China. His research interests include ac/dc microgrids, grid-connected converters for renewable energy systems and DGs, model predictive control, power quality, multilevel converters, ac motor control, and resonance suppression technique for smart grid applications. He is currently the supervisor for 11 master students, two of which have been nominated as provincial outstanding graduate student of UESTC. He has authored more than 20 SCIE-indexed journal papers and one book chapter in the area of power electronics, motor control, battery management system, and smart grid. He has seven issued and ten pending patents.

Dr. Long is an active Reviewer for the IEEE TRANSACTIONS ON POWER ELECTRONICS, *ISA Transactions*, *Applied Energy*, *Energy*, the IEEE TRANSACTIONS ON SMART GRID, IEEE TRANSACTIONS ON INDUSTRIAL ELECTRONICS, IEEE TRANSACTIONS ON SUSTAINABLE ENERGY, and IEEE TRANSACTIONS ON ENERGY CONVERSION.

Tianxu Cao received the B.S. degree in electrical engineering from the University of Electronic Science and Technology of China, Chengdu, China, in 2020. He is currently working toward the Ph.D. degree in electrical engineering with Zhejiang University, Hangzhou, China.

His research interests include model predictive control of grid-connected inverters, modeling and control of grid connected converters, wide bandgap power conversion systems, and renewable energy generation systems.

Wenting Fang received the B.S. degree in electrical engineering and automation from the University of Electronic Science and Technology of China, Sichuan, China, in 2020.

Her main research interests include suppress dc component of transformerless *LCL*-type grid-connected inverter with virtual capacitors in weak grids, multilevel inverters, and renewable energy generation systems.

Kil To Chong (Member, IEEE) received the Ph.D. degree in mechanical engineering from Texas A&M University, College Station, TX, USA, in 1995.

He is currently a Professor and the Department Head of the School of Electronics and Information Engineering and a member and the Head of the Advanced Electronics and Information Research Center, Chonbuk National University, Jeonju, South Korea. His research interests include motor fault detection and control, network system control, sensor network systems, time-delay systems, and neural networks.

Josep M. Guerrero (Fellow, IEEE) received the B.S. degree in telecommunications engineering, the M.S. degree in electronics engineering, and the Ph.D. degree in power electronics from the Technical University of Catalonia, Barcelona, Spain, in 1997, 2000, and 2003, respectively.

Since 2011, he has been a Full Professor with the Department of Energy Technology, Aalborg University, Aalborg, Denmark, where he is responsible for the Microgrid Research Program. From 2014, he has been a Chair Professor with Shandong University; from 2015, he has been a Distinguished Guest Professor with Hunan University; and from 2016, he has been a Visiting Professor Fellow with Aston University, Birmingham, U.K.; and a Guest Professor with the Nanjing University of Posts and Telecommunications, Nanjing, China. From 2019, he has been a Villum Investigator by The Villum Fonden, Søborg, Denmark, which supports the Center for Research on Microgrids, Aalborg University, being the founder and Director of the same center. His research interests include different microgrid aspects, including power electronics, distributed energy-storage systems, hierarchical and cooperative control, energy management systems, smart metering and the Internet of Things for ac–dc microgrid clusters and islanded minigrids. He has authored or coauthored more than 600 journal papers in the fields of microgrids and renewable energy systems, which are cited more than 50 000 times. His research specially focuses on microgrid technologies applied to offshore wind, maritime microgrids for electrical ships, vessels, ferries and seaports, and space microgrids applied to nanosatellites and spacecrafts.

Prof. Guerrero is an Associate Editor for a number of IEEE transactions. He was the recipient of the Best Paper Award of the IEEE TRANSACTIONS ON ENERGY CONVERSION for the period 2014–2015, the best paper prize of IEEE-PES in 2015, and the Best Paper Award of the *Journal of Power Electronics* in 2016. During six consecutive years, from 2014 to 2019, he was awarded by Clarivate Analytics (former Thomson Reuters) as Highly Cited Researcher with 50 highly cited papers. In 2015, he was elevated as an IEEE Fellow for his contributions on "distributed power systems and microgrids."